Environmental Science
Processes & Impacts

Iron and iron-bound phosphate accumulate in surface soils of ice-wedge polygons in arctic tundra

Journal:	*Environmental Science: Processes & Impacts*
Manuscript ID	EM-ART-03-2020-000142.R1
Article Type:	Paper

SCHOLARONE™
Manuscripts

Iron and iron-bound phosphate accumulate in surface soils of ice-wedge polygons in arctic tundra

Authors: Elizabeth Herndon[1,2*], Lauren Kinsman-Costello[3], Nicolle Di Domenico[2], Kiersten Duroe[2], Maximilian Barczok[2], Chelsea Smith[3], Stan D. Wullschleger[1]

[1]Environmental Sciences Division, Oak Ridge National Laboratory, Oak Ridge, TN
[2]Department of Geology, Kent State University, Kent, OH
[3]Department of Biological Sciences, Kent State University, Kent, OH

*corresponding author: herndonem@ornl.gov

Submitted to Environmental Science: Processes and Impacts
Special Issue: Cryosphere Chemistry

This manuscript has been authored in part by UT-Battelle, LLC, under contract DE-AC05-00OR22725 with the US Department of Energy (DOE). The US government retains and the publisher, by accepting the article for publication, acknowledges that the US government retains a nonexclusive, paid-up, irrevocable, worldwide license to publish or reproduce the published form of this manuscript, or allow others to do so, for US government purposes. DOE will provide public access to these results of federally sponsored research in accordance with the DOE Public Access Plan (http://energy.gov/downloads/doe-public-access-plan)

Abstract

Phosphorus (P) is a limiting or co-limiting nutrient to plants and microorganisms in diverse ecosystems that include the arctic tundra. Certain soil minerals can adsorb or co-precipitate with phosphate, and this mineral-bound P provides a potentially large P reservoir in soils. Iron (Fe) oxyhydroxides have a high capacity to adsorb phosphate; however, the capacity for Fe oxyhydroxides to adsorb phosphate and limit P bioavailability in organic tundra soils is not known. Here, we examined the depth distribution of soil Fe and P species in the active layer (< 30 cm) of low-centered and high-centered ice-wedge polygons at the Barrow Environmental Observatory on the Alaska North Slope. Soil reservoirs of Fe and P in bulk horizons and in narrower depth increments were characterized using sequential chemical extractions and synchrotron-based x-ray absorption spectroscopy (XAS). Organic horizons across all polygon features (e.g., trough, ridge, and center) were enriched in extractable Fe and P relative to mineral horizons. Soil Fe was dominated by organic-bound Fe and short-range ordered Fe oxyhydroxides, while soil P was primarily associated with oxides and organic matter in organic horizons but apatite and/or calcareous minerals in mineral horizons. Iron oxyhydroxides and Fe-bound inorganic P (P_i) were most enriched at the soil surface and decreased gradually with depth, and Fe-bound P_i was > 4× greater than water-soluble P_i. These results demonstrate that Fe-bound P_i is a large and ecologically important reservoir of phosphate. We contend that Fe oxyhydroxides and other minerals may regulate P_i solubility under fluctuating redox conditions in organic surface soils on the arctic tundra.

Environmental Significance Statement

The arctic tundra stores large quantities of soil carbon that can be released to the atmosphere as greenhouse gases as tundra soils warm. Phosphorus is a limiting nutrient to plants and microorganisms in many ecosystems including the arctic, and its bioavailability could influence plant growth (increased carbon storage) and decomposition (decreased carbon storage), and thus impact the rate and magnitude of greenhouse gas emissions from these carbon-rich ecosystems. Here, we examine how iron oxide minerals affect the solubility and potential bioavailability of phosphorus in tundra soils.

1. Introduction

Rising atmospheric carbon dioxide (CO_2) and global temperatures enhance plant growth and alter plant community composition. Increased plant growth may partially offset anthropogenic CO_2 additions by removing CO_2 from the atmosphere and increasing the amount of C stored in terrestrial ecosystems (summarized in Ciais *et al.*[1]; however, plant growth and carbon uptake is constrained by nutrient (e.g., N and P) availability in the soil[2-4]. Soil microorganisms, which may increase in biomass and/or activity in a warming climate, can either compete with plants for available nutrients or deliver nutrients to plants through mutualistic relationships[5-7]. Although N is often implicated as the primary limiting nutrient to terrestrial ecosystems at high latitudes (e.g., Du *et al.*[8]), P is frequently limiting or co-limiting in arctic tundra[6, 9, 10], particularly in low-lying wet sedge regions, and can modulate ecosystem response to N additions[11]. Furthermore, arctic freshwater ecosystems are primarily P limited[12, 13], possibly due to preferential retention of P relative to N on arctic hillslopes[14].

Tundra ecosystems are particularly sensitive to changing climate, both because biogeochemical reactions are limited by cold temperatures and because temperatures at high latitudes are warming more rapidly than anywhere else on the planet[15]. Tundra soils, which typically contain permafrost within the top meter and undergo annual freeze-thaw cycles, are characteristically organic-rich due to slow decomposition of organic matter. Tundra landscapes are also often water-logged because shallow permafrost inhibits vertical water flow; however, soil saturation varies in response to seasonal climate and as a function of local topography.

Adding to the complexity of biological competition, P, which is bioavailable as the inorganic anions HPO_4^{2-} and $H_2PO_4^-$, strongly adsorbs to soil minerals such as Fe and Al oxides through inner-sphere complexes[16, 17]. In many Fe- and Al-rich temperate and tropical soils, P bioavailability declines over time due to P leaching coupled with increasing sorption to oxides[18, 19]. Given that organic soils are prevalent across the tundra, particularly in the active layer of arctic soils, mineral interactions and the ecological roles of mineral-derived elements are often overlooked in these systems. However, multiple studies implicate Fe as a driver of ecosystem function in tundra soils, particularly with respect to carbon cycling.

The wet, organic-rich conditions that characterize the tundra also facilitate dynamic Fe biogeochemistry. Redox gradients generated by variable saturation, both vertically within soil profiles and laterally across topographic features, drive microbially mediated Fe oxide dissolution and precipitation[20-22]. Microbial mats dominated by Fe oxidizing bacteria are a dominant feature of many tundra soils where low temperatures and moderately acidic pH favor microbial Fe oxidation by slowing the kinetics of abiotic processes[22]. Dissimilatory Fe reduction, in which microbes use organically complexed Fe(III) and Fe (III) oxides as terminal electron acceptors for respiration, is a major metabolic pathway for CO_2 production in anoxic soils[23-25] and has been linked to increased anaerobic methane oxidation[26]. High concentrations of dissolved organic matter can stabilize dissolved Fe^{3+} and colloidal Fe in soil solution[27]. Additional CO_2 is generated by the abiotic oxidation of aqueous Fe^{2+} to Fe^{3+}, which produces hydroxyl radicals that non-selectively degrade organic matter[28, 29]. Iron oxides can conversely preserve organic matter and inhibit decomposition through sorption or co-precipitation, even forming coatings around particulate organic matter[30, 31].

Iron cycling is well known to regulate P solubility in lakes and lower latitude wetlands. Phosphate release from sediments into the water column is limited by oxidized Fe at the sediment-water interface but increases under transient anoxia that drives Fe oxide dissolution[32-34]. Iron oxides have also been shown to sequester phosphate in well-drained, Fe-rich temperate and tropical soils, but sorption capacity does not necessarily indicate bioavailability. For example, soil microorganisms can effectively compete for soluble phosphate when microbial demand is high, limiting partitioning on mineral surfaces[35]. Furthermore, although transient drops in redox potential are expected to mobilize P from soil oxides[36], microbial P uptake and utilization can be limited under reducing conditions due to low phosphatase activity that limits P acquisition from organic compounds[37]. Similar observations of Fe-P interactions do not exist for organic-rich tundra soils. Phosphorus is presumed to cycle primarily between soil microorganisms and tundra plants that release phosphatase enzymes to cleave phosphate from soil organic matter[6, 38]; however, dynamic Fe redox cycling has the potential to regulate phosphate solubility. In order to investigate

complex interactions between redox conditions, geochemical processes, and biological uptake in arctic ecosystems, it is necessary to examine major Fe and P reservoirs in tundra soils.

In a previous study, we evaluated Fe and P geochemistry in organic surface soils across multiple tundra and boreal sites[39]. We found that Fe oxyhydroxides accumulate in organic horizons of low-lying soils and confer a high capacity for those soils to bind phosphate. In these surface soils, differences in Fe accumulation and phosphate sorption capacity were more pronounced across hillslopes than among microtopographic features. Here, we extend our study beyond surface soils to examine changes in Fe and P geochemistry with depth in the seasonally thawed active layer of polygonal tundra. It is necessary to evaluate Fe-P interactions as a function of soil depth in order to obtain a more complete understanding of potential P bioavailability and storage in soil profiles. Tundra plants have unique and stratified root networks that acquire nutrients from different depths[40-42], and nutrients mobilized at depth can diffuse upwards and be accessed by plants and microorganisms in shallow soils. Nutrient acquisition from depth may become increasingly important as permafrost thaw releases readily bioavailable nutrients into solution[43].

To understand how soil Fe and P vary with depth and microtopography, we examined active layer soils obtained from different microtopographic features of high-centered and low-centered ice-wedge polygons in the Barrow Environmental Observatory on the Alaska North Slope. We hypothesized that Fe oxides and Fe-bound phosphate would be most enriched at the interface between organic and mineral soil horizons, a presumed redox boundary, due to oxidation of Fe^{2+}-rich soil solution and subsequent adsorption of phosphate by precipitated Fe phases. Sequential chemical extractions were coupled with x-ray absorption spectroscopy to identify major Fe and P soil reservoirs.

2. Methods

2.1. Site description and soil collection

The Barrow Environmental Observatory (BEO) is located outside of Utqiaġvik, AK in the coastal

region of the Alaska North Slope and has been a focus of the Next Generation Ecosystem Experiments (NGEE-Arctic)[44]. Annual precipitation at the BEO is ~12 cm with an additional 75 cm of snowfall (1901 to 2016[45]). Average annual air temperature is -12°C and the maximum daily temperature is below freezing from October through May. The seasonally thawed active layer deepens to approximately 30 – 50 cm by late summer and is underlain by continuous permafrost[24, 46]. This arctic coastal tundra ecosystem is characterized by an abundance of lake and interlake landscapes containing ice-wedge polygons[47]. High-centered polygons are elevated mounds with low-lying depressions surrounding the mounds. Low-centered polygons have a low-lying center with elevated rims surrounding the depressed center. These polygons regulate hydrologic flow paths that form redox gradients across centimeter-scale depths[21, 48, 49]. Low areas including troughs are dominated by sedges (*Carex aquatilis*) and also contain lesser amounts of grasses (*Dupontia fisheri*) and forbs (*Petasites fridgidus*). Mosses (*Sphagnum spp.*) dominate high areas, which also contain sedges (*Eriophorum angustifolium, E. russeolum, E. vaginatum*)[48, 50].

Fifteen intact soil cores were collected from the active layer of low- and high-centered polygons on October 15, 2015 at the NGEE intensive field site at the BEO (Figure 1). The length of each soil core spanned the active layer at the time of sampling but did not capture maximum thaw depth. Samples were obtained using a slide hammer equipped with a split soil core sampler (AMS, Inc., American Falls, Idaho). Core depths were reported from the surface of the soil to the sampling depth and ranged from 12.0 cm to 29.5 cm (Table 1). From the high-centered polygon, cores were collected from microtopographic features including the center (high-centered polygon center; HC-Center) and trough (high-centered polygon trough; HC-Trough). From the low-centered polygon, cores were collected from microtopographic features including the center (low-centered polygon center; LC-Center), ridge (low-centered polygon ridge; LC-Ridge), and trough (low-centered polygon trough; LC-Trough) features. Three replicate cores were obtained from each location. Once collected, each core was measured for length, photographed, wrapped in aluminum foil, labelled, sealed in plastic bags, and temporarily stored in a -30°C walk-in freezer at the Barrow Arctic Research Center (BARC). Samples were later packed in

blue ice, shipped overnight to Kent State University, and immediately stored in a -20°C freezer until processing. Soils were frozen to inhibit microbial activity and oxidation of reduced species prior to analysis. Effects of freezing and thawing on soil properties, such as enhanced Fe oxide dissolution or precipitation in freeze-concentrated soil solution[51], were not investigated in this study but may be similar to *in situ* freeze-thaw cycles.

Frozen soil cores were thawed and processed in a vinyl anaerobic chamber with N_2 atmosphere containing at least 1.0% H_2 and less than 1 ppm O_2. Soils were removed from their plastic bags and aluminum foil and placed onto a tray, where large roots and other green vegetation were removed. The organic-mineral interface was identified by visual color changes and textural contrast within each core and varied between 8 – 14 cm below ground surface (Table S1). Cores from the low centered-polygon center contained only organic horizons. Each core was sectioned into ~4 cm depth increments using a multipurpose oscillating power tool. The depth increments were homogenized and subsampled for later geochemical analysis (Table S2). Within the anaerobic chamber, subsamples obtained from the depth increments were air-dried, lightly ground with a mortar and pestle, and stored in plastic sample bags. Remaining wet soil from each depth increment was homogenized by horizon and partitioned into subsamples for physical and chemical characterization (described below). Results from soil characterization described below are provided in the supporting information (Tables S1 and S2) and in an online database[52].

2.2. Soil characterization

2.2.1. Bulk soil properties

Soil pH was measured in slurries of 1.0 ± 0.05 g dry soil and 5 ml of N_2-degassed potassium chloride solution (1 M KCl) mixed in the anaerobic chamber[53]. Soil slurries were shaken by hand, left to stand for 10 min, removed from the anaerobic chamber, and then measured for pH using a benchtop pH meter (± 0.01). Gravimetric water content (g H_2O g dry soil^{-1}) was determined from the mass loss of field wet soil (~5 – 7 g) following drying in an oven at 105°C for 24 hr[54]. Oven-dried triplicate soils were combined,

lightly ground with an agate mortar and pestle, and used for loss-on-ignition analyses. Loss-on-ignition (LOI, %), an approximate measure of soil organic matter, was determined from the mass loss of oven-dried soil (0.5 g) combusted at 550°C for 4 hours. Subsamples of each soil horizon were finely ground in a SPEX 8000M ball mill with tungsten carbide vials for 5 minutes, and the resulting powders (~5 – 7 mg) were loaded into tin capsules and analyzed for carbon and nitrogen concentrations via combustion on an Elemental Analyzer (Costech ECS 4010). Soil bulk density (ρ_b) was calculated as ln ρ_b (g cm^{-3}) = – [%SOC – 8.24] ÷ 9.79 following Bockheim et al.[55], and subsequently used to convert gravimetric water content to volumetric water content (cm^3 soil-cm^{-3}), assuming the bulk density of water to be approximately unity. All analyses were completed for duplicate or triplicate subsamples from each soil and quantified using appropriate instrument calibration curves. Soil properties for each soil feature are reported as the mean (± S.E.M.) of values obtained across three replicate soil cores.

2.2.2. Soil extractions

2.2.2.1. Bulk soil horizons

Iron was extracted from bulk soil horizons using a sequential extraction protocol designed to differentiate between iron oxide minerals and modified for use on peat soils to remove organic matter[56-58]. Extracts were chosen and sequentially ordered based on their reported selectivity for desired phases. For example, although both hydroxylamine hydrochloride and ammonium oxalate are used to extract SRO phases, oxalate extraction was performed separately here in order to selectively isolate magnetite, which is not extracted by hydroxylamine[58]. Hypochlorite extraction of organic matter was completed prior to mineral extractions so that organic-bound Fe would not be extracted along with Fe mineral phases. Sodium hypochlorite has been determined to remove organic matter while not significantly altering or dissolving iron oxide mineral phases[56].

First, exchangeable Fe was extracted with N_2-degassed barium chloride and ammonium chloride (0.1 M $BaCl_2$-NH_4Cl) solution within an anaerobic chamber. 10 ml of extraction solution was added to ~1.0 g

of thawed soil sample and mixed for 20 min on an end-over-end rotator. The slurry was centrifuged at 4000 rcf for 30 min, and the supernatant was filtered (<0.45 µm nylon syringe filter) into 50 ml metal-free Falcon tubes and acidified with 2-3 drop of 67-70% trace metal grade nitric acid[57]. All proceeding steps were performed outside of the anaerobic chamber. Organic-bound Fe was extracted with two rounds of 10 ml sodium hypochlorite (5-6% active Cl; acidified with 34-37% trace metal grade hydrochloric acid to pH 8) for 6 h each round. Short-range ordered (SRO) iron oxyhydroxides (i.e., ferrihydrite and lepidocrocite phases) were extracted with 10 ml of 1 M hydroxylamine-HCl in 25% v/v acetic acid for 48 h[58]. Next, crystalline iron (III) oxides (e.g., hematite and crystalline goethite) were extracted with freshly prepared citrate-buffered sodium dithionite (50 g L^{-1} sodium dithionite in 0.35 M acetic acid and 0.2 M sodium citrate buffer solution at pH 4.8) by mixing on the end-over-end rotator for 2 h. Finally, the magnetite (Fe_3O_4) fraction, which represented a small proportion of total Fe and was subsequently reported with dithionite-soluble Fe as *crystalline oxides*, was extracted with a 0.2 M ammonium oxalate and 0.17 M oxalic acid solution at pH 3.2 on the end-over-end rotator for 6 h. Between each sequential extraction step, soils were rinsed and vortexed with 10 ml 0.01 M KCl solution, then centrifuged at 4000 rcf for 30 min. Supernatants were filtered with a <0.45 µm syringe filter and combined with the extracts. All extracts and matrix standards were stored at 4°C until analyses.

Homogenized bulk soil horizons were also extracted with a sequential extraction protocol adapted for phosphorus fractionation[34, 59]. Briefly, ~1 g of wet soil was extracted with 25 ml N_2-degassed ultrapure water for 1 h on an end-over-end rotator in an anerobic chamber (water-soluble P). The slurry was centrifuged at 4000 rcf for 30 min, and the supernatant was filtered (< 0.45 µm nylon syringe filter) into 50 ml metal-free Falcon tubes and acidified with sulfuric acid. Second, Fe-oxide-bound P was extracted with 25 ml of deoxygenated 0.11 M bicarbonate-buffered dithionite solution for 1 hr. The extract was then aerated for 1 h and then acidified with 1 M sulfuric acid (H_2SO_4). Base-soluble P, primarily reflecting inorganic P associated with non-reducible oxides and organic P, was extracted with 25 ml of 0.1 M NaOH for 16 h. In the absence of Fe oxides, NaOH primarily extracts amorphous and crystalline Al minerals[60]. The base-extract was acidified with 1 M H_2SO_4 to precipitate humic compounds, which

were collected onto glass fiber filters, dried at 105°C to determine yield, and combusted at 520°C to determine organic content. Ashed material was digested with concentrated nitric acid on a hot block to extract humic P. Acid-soluble P associated with apatite and/or calcareous minerals was extracted from the soil residue with 25 ml of 0.5 M hydrochloric acid for 1 hr. For all steps, pellets were rinsed with 25 ml of deoxygenated ultrapure water between extractions, and rinse filtrates were combined with extracts prior to acidification. Water, dithionite, and base extracts were subsequently analyzed for *soluble reactive P* and *soluble non-reactive P*, as described below.

2.2.2.2. Soil depth increments

A two-step extraction procedure was used to quantify water-soluble and dithionite-soluble concentrations of Fe, Al, and P in soils sections into finer depth increments. These fractions represent operationally defined bioavailable (water-soluble) and iron-bound (dithionite-soluble) elements, although dithionite also extracts significant quantities of Al in amorphous minerals[60, 61]. Extractions were performed on ~1 g freeze-dried soil in an anaerobic chamber with N_2 (< 4% H_2) atmosphere. First, water-soluble P was extracted with 25 ml deoxygenated ultrapure water (18 MΩ), which was prepared by purging boiling water with N_2 gas for 1 h. The soil slurry was mixed for 1 h at 250 rpm on an end-over-end rotator, then centrifuged for 20 min at 4,000 rcf. Each supernatant was syringe filtered into a new centrifuge tube in the anaerobic chamber. The remaining soil pellet was rinsed with 25 ml deoxygenated ultrapure water, vortexed to mix, and centrifuged at 4,000 rcf for 10 min. The filtered rinse solution was combined with the initial extract, acidified with 1 ml of 1 M H_2SO_4, and stored at ~4°C until analysis. Second, total reducible Fe and associated Al and P were extracted with bicarbonate-buffered sodium dithionite (0.11 M $NaHCO_3$-$Na_2S_2O_4$), which has been shown to effectively extract iron oxides from sediments[62]. Freshly prepared (< 24 h) dithionite reagent (25 ml) was added to each soil pellet following the water extraction. Soil slurries were vortexed, rotated on an end-over-end rotator at 250 rpm for 1 h, then centrifuged for 20 min at 4,000 rcf. The supernatant was poured directly into a clean plastic bottle inside the anaerobic chamber. Each pellet was rinsed twice by adding 25 ml of deoxygenated ultrapure

water, vortexing, and centrifuging for 10 min at 4,000 rcf. The rinse was combined with the original extract, filtered (Whatman Glass Microfiber, 47 mm diameter, 0.7 μm pore size), and then aerated for 1 h outside of the anaerobic chamber. Each extract was then acidified with 5 ml 1 M H_2SO_4 prior to storage at ~4°C. In all steps, vortexing and centrifugation were conducted in sealed tubes outside of the anaerobic chamber.

2.2.2.3. Soil extract analysis

Element concentrations (Fe, Al, P) in extract solutions were analyzed by inductively coupled plasma optical emission spectrophotometry (PerkinElmer 8000, ICP-OES) at emission wavelengths of 238.204 nm, 396.153 nm, and 213.617 nm, respectively. Soluble reactive phosphorus (SRP), typically used as a proxy for orthophosphate and referred to as inorganic P (P_i) in this study, was measured in water-, dithionite-, and hydroxide-extracts by reacting an aliquot of filtered solution with PhosVer 3 reagent (Hach) and measuring absorbance at 880 nm on a UV-Visible spectrophotometer (Shimadzu UV-1800). Non-reactive P, typically used as a proxy for organic P and inorganic P species other than orthophosphate, was calculated as the difference between total P and P_i in filtered solutions. Non-reactive P was assumed negligible when P_i values exceeded total P in solution. Total P was used to represent P_i for two core soils (HCT 0 – 4 cm and 4 – 8 cm) for which measured P_i concentrations were much higher than total P. For all analyses, calibration standards were prepared in the matrix solution for each extract. Method blanks were analyzed to evaluate potential contamination from extraction chemicals. For concentrations below the limit of quantification, a value equal to one-half the lowest calibration standard was used in calculations. Element concentrations in extract solutions were converted to dry weight soil concentrations. For extractions performed on wet soil, i.e., Fe and P extractions of bulk soil horizons, gravimetric water content (g H_2O g-dry-soil^{-1}) was used to convert wet soil mass to dry soil mass.

Element pools in each horizon (mmol m^{-2} cm^{-1}) are reported as element mass per square meter of land surface per centimeter of soil depth. The element pools are reported per unit soil depth rather than for the entire horizon 1) in order to better compare horizons of varying thickness, and 2) because the thaw depth

at the time of sampling was shallower than the maximum active layer thickness. Element pools were quantified by averaging the product of element concentration (mmol kg^{-1}), soil bulk density (kg m^{-3}), and horizon thickness (m), then dividing by horizon thickness (cm) for each soil horizon. This calculation provides the mass of each soil constituent in a $1m^2$ x 1cm thick soil layer.

2.2.3. Phosphate sorption index

The phosphate sorption index (PSI) is a single-point adsorption value that provides a comparative measure of phosphate adsorption capacity across soils[63]. Here, ~4 g of wet soil from each soil horizon were weighed into 50 ml metal-free centrifuge tubes in the anaerobic chamber. Each soil was mixed with 20 ml of 75 mg L^{-1} P solution (as KH_2PO_4) and placed on an end-over-end rotator for 24 h. The slurry was filtered through a 0.45 µm Supor filter with a 0.7 µm glass fiber prefilter. Dissolved phosphate, represented by molybdate reactive P, was measured using the molybdate blue method by reacting a 100× diluted aliquot of the filtered solution with PhosVer 3 reagent (Hach) and measuring absorbance at 880 nm on a UV-Visible spectrophotometer (Shimadzu UV-1800). Absorbance values were converted to concentrations using a linear regression of absorbance as function of concentration in calibration standards (0.007 – 0.815 mg L^{-1} P as KH_2PO_4). Phosphate sorbed or released by the soil was calculated as the difference between the phosphate concentration of initial solution and final dissolved phosphate. The residual soil was dried at 105°C for 24 h to determine dry soil mass (g). The amount of PO_4^{3-} sorbed to the soil (P_{sorbed}; mg g^{-1}) was calculated as the difference between the initial and final dissolved PO_4^{3-} mass in solution normalized to the dry soil mass. The phosphate sorption index (PSI) is calculated as the ratio of sorbed P to dissolved P[63]:

$$PSI = 100 \times \frac{P_{sorbed}}{\log\left(P_{dissolved}\right)}$$

Here, $P_{dissolved}$ (µmol L^{-1}) is the final concentration of dissolved P (as phosphate) in solution.

2.2.4. X-ray absorption spectroscopy

X-ray absorption spectroscopy was conducted at beamline 12-BM at the Advanced Photon Source (APS) in March 2018. Soils, previously dried under N_2/H_2 atmosphere and transported to APS in AnaeroPaks™, were packed into Teflon sample holders and sealed with Kapton tape inside an Ar-filled anaerobic chamber. XAS spectra were collected from -150 eV to +547 eV around the Fe K-edge (~7112 eV) with a 500 μm wide beam at 4 x 10^{11} photons s^{-1} (@ 12 keV). Detectors included a N_2-filled Ionization Chamber for transmission and a Canberra 13 element detector for fluorescence. Three to five scans positioned 0.6 mm apart were collected for each sample to account for possible heterogeneity. Data processing, including alignment, merging of replicate scans, and linear combination fits, was completed in Athena (version 0.9.26)[64]. Spectra were shifted -0.95 eV to align an Fe foil (E_0 = 7111.6 eV) measured during the experiment with the Fe foil (E_0 = 7110.6 eV) reported in an Fe reference library. All merged and processed spectra are provided in supporting information (Tables S3 and S4).

Linear combination fits (LCFs) to determine average oxidation state were performed in XANES from -20 to +30 eV using reference spectra for single valence compounds (ferrous oxalate, ferric oxalate, ferric citrate, goethite, and hematite). Linear combination fits to determine approximate speciation in bulk horizons were performed in EXAFS ($k^2\chi(k)$) from 3 to 10 $Å^{-1}$ using reference spectra for ferrous oxalate, ferric oxalate, ferric citrate, vivianite, biotite, chlorite, lepidocrocite, magnetite, ferrihydrite, and goethite. Best fits were selected to contain the lowest number of components and minimize reduced chi-square and R-factor values. That is, additional components were not included in fits unless they improved the best fit parameters by at least 20%. Reference spectra that best fit the bulk horizon spectra (ferrihydrite, ferrous oxalate, ferric oxalate, ferric citrate, and chlorite) were used in LCFs for the core samples. All processed spectra and fits are provided in the supporting information (Tables S3 and S4) and in an online database[52].

2.2.5. Data analysis

Error is reported for all values as either the analytical error for individual measurements or as the standard error of the mean for averages of multiple measurements. Significant differences in soil properties were evaluated between organic and mineral horizons and across topographic features (high or

low) using a two-way ANOVA with a Tukey post-hoc test for interactions ($\alpha = 0.05$) in OriginPro® software. Microtopographic high features included the center of the high-centered polygon (HCC) and the ridge of the low-centered polygon (LCR). Topographic low features included the trough of the high-centered polygon (HCT) and the center (LCC) and trough (LCT) of the low-centered polygon. Significant correlations between variables across all samples were determined using Pearson correlation (r; $\alpha = 0.05$).

3. Results and Discussion

3.1. Organic and mineral soil properties

Soils in the high-centered and low-centered polygon were acidic and organic-rich with saturation that varied by microtopography. High and low features differed in volumetric water content between organic horizons (Figure 2). Organic horizons in the elevated features were drier (< 0.15 $cm^3\ cm^{-3}$) than in the low features (0.45 ± 0.21 $cm^3\ cm^{-3}$) ($p = 0.001$), which drove lower average volumetric water content in organic (0.33 ± 0.05 $cm^3\ cm^{-3}$) than in mineral (0.44 ± 0.05 $cm^3\ cm^{-3}$) horizons ($p = 0.03$). Water content was similar between the organic and mineral horizons in topographic lows, consistent with a water table that inundates low features but is present only in the subsurface of raised features[65]. Topographic lows are consequently oxygen-depleted within a few centimeters of the soil surface whereas high features maintain high oxygen saturation[20].

Soil organic C (SOC) and N (SON) were higher in the organic horizons (31.9 ± 2.8 wt.% C and 1.45 ± 0.12 wt.% N) than in the mineral horizons (16.5 ± 2.8 wt.% C and 0.75 ± 0.05 wt.% N) ($p < 0.001$) (Table 1), with similar C/N ratios between horizons (21.8 ± 0.7 for organic and 21.2 ± 2.6 for mineral). Soil organic C was slightly higher in the organic horizons of raised features (39.5 ± 3.6 and 42.5 ± 0.5 wt.% C for HCC and LCR, respectively) than microtopographic lows (< 33 wt.% C). Organic horizons in low features may have higher mineral contents due to cryoturbation or sediment runoff from high features[55].

Soil pH differed across individual features but was similar between horizons within features (Figure 2). Namely, ridge and center soils were more acidic (< 4.5) than trough soils (4.5 < pH < 5.5). Troughs, which comprise the drainage network in this landscape[66], are likely buffered by higher concentrations of base cations that leach from raised features. Alternatively or in conjunction to this explanation, higher pH could derive from anaerobic respiration pathways that consume protons and produce alkalinity[67]. For example, Fe(III)-reduction is a major anaerobic respiration pathway in BEO soils[20, 23, 24]. Soil pH in the low features was slightly more acidic than values reported for pore water (~5 to 6)[49], likely due to retention of exchangeable H^+ on particle surfaces that were not released into soil solution.

3.2. Iron speciation by horizon and microtopography

Soil Fe decreased and shifted from relatively labile exchangeable and organic-bound species to oxide phases with depth. Organic horizon soils contained over twice as much extracted Fe (362 ± 69 mmol kg^{-1}) as mineral horizons (152 ± 11 mmol kg^{-1}), primarily as organic-bound (42 ± 5%) and SRO Fe oxides (35 ± 5%) with lesser amounts of exchangeable Fe (16 ± 4%) and minimal crystalline Fe oxides (7 ± 2%) (Figure 3; Table 2). Mineral horizons contained proportionally more crystalline oxides (14 ± 2%) but less organic-bound Fe (29 ± 5%) ($p < 0.05$), with similar proportions of SRO Fe oxides (37 ± 5%) and exchangeable Fe (20 ± 7%). As detailed in section 3.4 below, Fe in organic horizons was most enriched in the shallowest soil and decreased with depth.

Across organic horizons, microtopography drove differences in Fe speciation that were similar to, but less pronounced than, trends observed across hillslope gradients[39]. Organic-bound Fe was enriched in topographic highs (195 ± 45 mmol kg^{-1}) relative to low features (104 ± 17 mmol kg^{-1}) ($p < 0.05$). Upland soils have been observed to contain relatively high proportions of organic-bound Fe due to acidic conditions that favor organic-complexation[39, 68-70]. Similarly, we observed consistently acidic pH (~ 4) for high features, particularly relative to trough soils (pH ~ 5). Although low features contained less organic-bound Fe than high features, low features did not contain substantially more SRO oxides than high features, as has been reported for low-lying soils along hillslopes[39]. Rather, minor variation in topography

and relatively acidic conditions likely precluded substantial variation in Fe speciation across this landscape.

Exchangeable Fe did vary by topographic position and was > 12× more abundant in low (79.5 ± 18.0 mmol kg^{-1}) than in high features (6.3 ± 2.0 mmol kg^{-1}) ($p = 0.001$) (Figure 3), consistent with differences in soil saturation (Figure 2). Low and wet soils are expected to favor reducing conditions that drive Fe oxide dissolution, generating dissolved Fe^{2+} or Fe^{2+} sorbed onto mineral surfaces. Iron oxide dissolution, which consumes protons, could also explain higher pH in the troughs[21, 67]. Exchangeable Fe in this study was higher than previously reported for analogous soils collected in April prior to spring thaw (< 15 mmol kg^{-1})[30]. We attribute this discrepancy to differences in when the cores were collected, i.e., April in the previous study versus October in this study. Exchangeable Fe concentrations likely increased between April to October due to persistently reducing conditions over the thaw season, as previously observed for soils in nearby drained thaw lake basins[20, 21]. Although high evaporation in the centers of low-centered polygons can dry surface soils and generate oxidizing conditions into late summer[21, 65], troughs comprise the drainage network for this landscape and remain relatively saturated.

Average Fe oxidation state, as determined by LCFs to the XANES region, was slightly higher in soils from the organic (2.88 ± 0.02) than mineral (2.81 ± 0.02) horizons ($p = 0.003$), and first-derivative peaks (E^0) for organic soils were correspondingly higher than their mineral counterparts (Table 3). The well-drained organic horizon of the HCC had the highest oxidation state (2.89) while the saturated mineral horizon of the LCT had the lowest (2.68). Spectra and positions of the first-derivative peaks (E^0) of all soils were generally consistent with spectra of organic-bound Fe(III) and Fe(III)-oxides[71]. All EXAFS spectra were best fit by a combination of organic-bound Fe (Fe(II)-oxalate, Fe(III)-oxalate, and Fe(III)-citrate), ferrihydrite, and chlorite. Averaged across all depths, organic-bound Fe (36 ± 5%) and ferrihydrite (45 ± 2%) were present in nearly equal proportions, consistent with sequential extraction results. Chlorite, an Fe(II)-bearing aluminosilicate that would not have been dissolved during sequential extraction, comprised the remaining 19 ± 2% of total Fe. Other less abundant constituents did not meaningfully improve the linear combination fits and are not reported here.

We further evaluated differences between horizons by calculating element storage in organic and mineral horizons. Due to higher bulk densities that compensated for lower element concentrations, mineral horizons contained higher quantities of organic-bound Fe (207 ± 30 vs 120 ± 21 mmol m^{-2} cm^{-1}; p = 0.04), SRO Fe oxides (379 ± 92 vs 204 ± 74 mmol m^{-2} cm^{-1}; p = 0.04), and crystalline Fe oxides (162 ± 45 vs 52 ± 22 mmol m^{-2} cm^{-1}; p = 0.01) than organic horizons, while exchangeable Fe was more similar between horizons (154 ± 64 vs 84 ± 32 mmol m^{-2} cm^{-1}; n.s.). These differences indicate that mineral horizons, although having low Fe concentrations relative to organic horizons, still contain a substantial store of these Fe phases.

3.3. Phosphorus speciation by horizon and microtopography

Soil P concentrations and major P-bearing phases differed by horizon but not across topographic features (Figure 3). Total extracted P was higher in organic (13 ± 2 mmol kg^{-1}) than mineral horizons and was comprised primarily of organic P (27 ± 5%) and P_i bound to reducible (20 ± 3%) and non-reducible (34 ± 5%) oxides. Acid-soluble P (16 ± 7%) was variable and increased with increasing bulk density (r = 0.82; $p < 0.001$), from which we infer that high concentrations of acid-soluble P correlated to high mineral content in organic horizons. Mineral horizons contained lower concentrations of total extracted P (8.1 ± 0.3 mmol kg^{-1}), which included a high proportion of acid-soluble P (46 ± 10%) and lower proportions of organic P (31 ± 6%) and P_i bound to reducible (5.5 ± 1.3%) and non-reducible (14 ± 2%) oxides. Water-soluble P_i comprised a small fraction of extracted P in both organic (3.3 ± 1.1%) and mineral (2.7 ± 2.4%) horizons.

Inorganic P associated with mineral oxides comprised the majority of P extracted from organic horizons (54 ± 8%) and a high proportion of P extracted from mineral horizons (20 ± 3%). Excluding organic P, oxide-bound P_i comprised ~80% of total inorganic P in organic horizons and 30% in mineral horizons, with the rest primarily contained in the acid-soluble P fraction. From these results, we determine that oxide-bound P_i is a critical but dynamic reservoir of P in these soils, particularly in organic horizons. Dithionite-soluble P_i, which was ~6x more abundant than water-soluble P_i, represents inorganic P bound

to reducible oxides such as ferrihydrite and goethite[58, 62]. This P_i could be released into solution during anoxic conditions that favor iron oxide dissolution, or conversely trapped during oxidizing conditions that favor precipitation. Base-soluble P_i, representing P_i bound to non-reducible oxides such as Al oxides, may represent a more recalcitrant P reservoir that remains inaccessible to plants and microbes regardless of redox conditions.

The abundance of these oxide-bound reservoirs in organic horizons is particularly notable given that oxide-bound P_i is often assumed inaccessible to microbes, and that biologically relevant P in arctic ecosystems is thought to primarily cycle between plants, microbes, and soil organic matter[6, 38, 72]. Rather, we propose that Fe-bound P is a significant fraction of soil P that is potentially bioavailable as redox conditions fluctuate. Reducing conditions drive dissolution of Fe oxides that either bind P directly or cement P-bearing aggregates[73]. Iron-bound P has similarly been implicated as a biologically relevant reservoir in tropical soils where redox fluctuations mobilize or immobilize organic C and inorganic P[36, 74]; however, the geochemical and biological interactions that control biological P uptake remain unclear. Microorganisms have been shown to effectively acquire soluble phosphate regardless of soil sorption strength, while sorption and microbial uptake combined can limit bioavailability to plants[35]. Furthermore, although Fe-bound P is released under reducing conditions and in theory more bioavailable to plants and microorganisms, uptake may be inhibited under anoxic conditions due to limited microbial assimilation[37].

Mineral horizons may serve as an important reservoir of P contained in calcareous minerals (extracted as acid-soluble P) that becomes nominally bioavailable during mineral weathering. Following the classic model for soil P redistribution with soil age[18, 19], P released from calcareous minerals could be taken up by plants or microbes and incorporated into soil organic P, or once solubilized, adsorbed onto oxide surfaces. Consistent with this classic model, Giblin et al.[72] observed decreases in calcareous P and increases in oxide-bound P_i with increased soil weathering in tundra on the foothills region of the North Slope. In our study, calcareous P was higher in mineral than organic horizons. Phosphorus release from these calcareous minerals, both in the organic and mineral horizons, may be enhanced by mycorrhizal fungi that exude protons and organic acids to accelerate mineral dissolution[5, 75]. Plants can then redistribute P from

depth to shallow soils[76], where it associates with organic matter or is adsorbed to oxide surfaces. Thus, the typical pattern for P redistribution with age is also observed as a function of soil depth.

When evaluating total horizon storage, organic horizons contained higher amounts of water-soluble reactive phosphate (0.56 ± 0.30 mmol m^{-2} cm^{-1}) than mineral horizons (0.19 ± 0.04 mmol m^{-2} cm^{-1}). Dithionite-soluble and base-soluble P_i pools were similar between organic (2.18 ± 0.44 mmol m^{-2} cm^{-1} and 4.71 ± 1.20 mmol m^{-2} cm^{-1}) and mineral (1.81 ± 0.59 mmol m^{-2} cm^{-1} and 5.28 ± 1.28 mmol m^{-2} cm^{-1}) horizons. Conversely, mineral horizons contained larger pools of acid-soluble P (26.4 ± 9.6 vs 9.47 ± 7.21 mmol m^{-2} cm^{-1}) and organic P (10.9 ± 3.2 vs 5.36 ± 1.60 mmol m^{-2} cm^{-1}).

The PSI, a comparative measure of soil phosphate adsorption capacity, was higher in the organic (63 ± 8 units) than mineral (39 ± 3 units) horizons ($p = 0.03$). PSI was relatively uniform across mineral horizons but variable across organic horizons, decreasing from the low-centered trough (86 ± 29) and ridge (80 ± 11), to the high-centered trough (63 ± 16) and low-centered center (51 ± 11), to the high-centered center (34 ± 6) (Table 4). Across all soils, PSI was strongly positively correlated with dithionite-soluble P_i ($r = 0.85$; $p < 0.0001$) and base-soluble P_i ($r = 0.80$; $p < 0.0001$), reflecting the ability of these soils to adsorb phosphate onto oxide minerals, particularly in organic horizons. PSI was also correlated with factors associated with physical and chemical differences between the horizons, i.e., bulk density ($r = -0.49$; $p = 0.01$), organic-bound Fe ($r = 0.59$; $p = 0.002$), carbon ($r = 0.54$; $p = 0.005$), and nitrogen ($r = 0.61$; $p = 0.001$).

3.4. Chemical depth profiles

Iron and P speciation were evaluated as a function of depth using x-ray absorption spectroscopy and a simplified chemical extraction scheme. Soils were examined in finer depth increments (~ 4 cm) than those available for the bulk horizons. Across all cores, the white line peak for Fe XANES was shifted to higher energies in organic than in mineral soils (Figure 4), indicating a higher proportion of oxidized Fe species that is consistent with higher E^0 values for bulk organic horizons (Table 3). Organic soils from the high-centered polygon center (HC-Center) exhibited strong white line peaks at ~7138 eV (Table 3), indicating

predominant oxidized Fe; however, fits to these soils were poor and individual components could not be reasonably resolved. All soils from other features were best fit by approximately equal proportions of organic-bound Fe(III) and ferrihydrite with small contributions of chlorite (Figure 4), similar to bulk horizons. Although spectra for mineral horizons were distinct from organic horizons, typically exhibiting steeper absorption edges and sharper peaks, differences in speciation could not be resolved with the linear combination fits. Consequently, no strong trends in calculated oxidation state or speciation were observed with depth.

Dithionite-soluble Fe was most enriched near the soil surface and decreased with depth, consistent with the accumulation of short-range ordered and/or crystalline Fe oxides in organic horizons (Figure 5). In contrast, concentrations of dithionite-soluble Al extracted from amorphous Al minerals did not vary with depth, indicating that Fe enrichment near the surface cannot be explained by mixing of minerals into the organic horizons through cryoturbation. In agreement with previous findings[30], the presence of Fe oxides in surface organic soils is more consistent with secondary oxide precipitation than with inputs of parent minerals from deeper soils through cryoturbation. We expect that dissolved Fe^{2+} is released into solution during reductive dissolution of Fe oxides in deep anoxic soils, migrates upwards, and is oxidized to generate Fe oxyhydroxides and organic-bound Fe (III) at the redox interface[27, 77]. In these organic-rich soils, associations between Fe precipitates and organic matter may facilitate long-term accumulation of SRO Fe oxides. For example, co-precipitation of organic matter with ferrihydrite can slow reductive dissolution and inhibit transformation to more crystalline phases at low C/Fe ratios[78, 79].

We hypothesized that dithionite-soluble Fe would be most enriched in the deepest organic soil, i.e., at the interface between the organic and mineral horizons. However, Fe concentrations were highest in the shallowest soils, from which we infer that the redox boundary is near to the soil surface. Oxygen diffusion into these surface soils may be limited by their high water content and by high concentrations of dissolved organic matter that increase biological oxygen demand. Furthermore, plant activity may drive dynamic redox cycling within shallow soils. Root exudation of labile C[80, 81] and radial oxygen loss from aerenchymous roots[82, 83] can enhance Fe oxide dissolution and reformation in surface soils where root

biomass is concentrated. Fine root biomass in tundra soils is concentrated in surface soils, with as much as 96% of root biomass in the top 30 cm, although certain plants such as sedges also root deeper the profile[50, 84].

The gradual rather than sharp decrease in dithionite-soluble Fe with depth could also result from a seasonally dynamic water table that periodically mobilizes and then reprecipitates Fe. Although the depth from the ground surface to the water table and redox interface is expected to vary across microtopographic features, we could not resolve differences between features in this study. We do note that two cores from the high-centered polygon showed less Fe enrichment near the surface, and one was enriched in dithionite-soluble Fe and P at depth (Figure 5; Figure S1), possibly reflecting the greater average depth to the water table relative to the low-centered polygon. Alternatively, concurrent enrichment of Al at that depth may indicate a particularly mineral-rich layer. Variation in depth trends may have obscured enrichment trends when averaged across multiple features.

Water-soluble P_i was concentrated in the surface soil and decreased sharply below 4 cm depth (Figure 5). Strong retention of water-soluble and nominally bioavailable P in the shallow soil likely derives from a biological control. Phosphorus enrichment in surface soils typically derives from nutrient uplift by plants, particularly in nutrient limited systems[76, 85]. Plant P is returned to the soil through organic matter decay, where is it released into solution as phosphate and subsequently available for plant or microbial uptake or mineral sorption. The water-soluble P_i measured here targeted soluble phosphate but also potentially represents P in microbial biomass. Microbial biomass P comprises a large proportion of potentially available P in arctic soils and can sometimes be released into solution during population crashes[6, 38, 72]. Although microbial biomass P is not water-extractable (e.g., Giblin et al.[72]), microbial cell lysis during freeze-thaw cycles associated with sample preparation may have released microbial P into solution[38].

Dithionite-soluble P_i was also most enriched in the surface soil but decreased gradually with depth and was more strongly correlated with dithionite-soluble Fe ($r = 0.53$; $p = 0.002$) than with water-soluble P_i ($r = 0.24$; n.s.). From this result, we infer a strong geochemical control on dithionite-soluble P_i that

derives primarily from association with Fe oxides. In fact, dithionite-soluble Al had no correlation with dithionite-soluble P_i ($r = 0.01$) despite being correlated with dithionite-soluble Fe ($r = 0.52$; $p = 0.002$). Phosphate released into solution through enzymatic cleavage from organic compounds can either be acquired by plants and microorganisms or associate with mineral surfaces. We demonstrate that a large proportion of P adsorbs to Fe oxyhydroxides, even in organic soils. In P-enriched surface soils (0 – 4 cm), dithionite-soluble P_i (6.82 ± 1.41 mmol kg^{-1}) was 3× higher than water-soluble P_i (2.21 ± 0.52 mmol kg^{-1}). In deeper soils (> 4 cm), the ratio of dithionite-soluble P_i (2.77 ± 0.82 mmol kg^{-1}) to water-soluble P_i (0.16 ± 0.07 mmol kg^{-1}) increased to ~17:1. One core from the high-centered trough had high concentrations of dithionite-soluble reactive P at depth; however, this enrichment was concurrent with abnormally high dithionite-soluble Fe (Figure S1).

4. Conclusions

Geochemical controls on nutrient phosphate solubility are still poorly understood in arctic ecosystems where organic soils dominate tundra landscapes. Dynamic Fe cycling across redox gradients within these soils has the potential to regulate phosphate solubility and influence P bioavailability by driving Fe oxyhydroxide formation and dissolution. Here, we investigated major Fe and P reservoirs and phosphate sorption capacity as a function of soil depth across polygon tundra with microtopographic variation (summarized in Figure 6). We found that both high-centered and low-centered polygons were dominated by organic-bound Fe and short-range ordered Fe oxyhydroxides that accumulated in shallow organic soils and conferred high phosphate sorption capacity. High proportions of inorganic P in shallow soils were associated with both reducible Fe oxides that are sensitive to redox fluctuations and may provide a transient P reservoir, and non-reducible oxides that are insensitive to redox fluctuations and may serve as a bio-inaccessible P reservoir. Indeed, 3× more inorganic P was associated with reducible Fe oxides than was present in solution in the shallow soil (top 4 cm), and the ratio of Fe-bound P_i to water-soluble P_i increased with depth. Water-soluble, and presumably bioavailable, inorganic P was present in low

concentrations at depth but was highly concentrated near the soil surface, indicating strong retention by plants and microorganisms.

Our study demonstrates that substantial amounts of inorganic P are associated with minerals in organic soils of the arctic tundra. In particular, substantial portions of inorganic P are associated with Fe oxyhydroxides in shallow soils. However, more research is needed to understand how geochemical reservoirs of Fe and P translate to bioavailability, especially under contrasting and/or fluctuating redox conditions that regulate Fe solubility. It is unclear whether adsorption to Fe oxyhydroxides inhibits P acquisition by biota, or conversely, if Fe-bound P_i could provide a transient P source depending on redox fluctuations. These considerations will better inform our understanding of how microorganisms and plants acquire the limiting nutrient P, and how bioavailability that constrains growth and land-atmosphere carbon budgets may shift under future climate scenarios.

Conflicts of Interest

The authors declare no conflicts of interest.

Acknowledgements

This research was funded by National Science Foundation grant EAR-1609027 (Geobiology and Low-temperature Geochemistry) to Herndon and Kinsman-Costello. NGEE Arctic is funded through the Department of Energy (DOE) Office of Science, Biological and Environmental Research (BER) program (ERPK757). This research used resources of the Advanced Photon Source, a U.S. Department of Energy Office of Science user facility operated for DOE Office of Science by Argonne National Laboratory under contract DE-AC02-06CH11357. X-ray absorption spectra were collected at sector 12BM with support from Benjamin Reinhart.

References

1. Ciais P, Sabine C, Bala G, Bopp L, Brovkin V, Canadell J, et al. Carbon and other biogeochemical cycles. Climate change 2013: the physical science basis. Contribution of Working Group I to the Fifth Assessment Report of the Intergovernmental Panel on Climate Change.; 2013.
2. Wieder WR, Cleveland CC, Smith WK, Todd-Brown K. Future productivity and carbon storage limited by terrestrial nutrient availability. Nature Geoscience. 2015;8(6):441-4.
3. Salmon VG, Soucy P, Mauritz M, Celis G, Natali SM, Mack MC, et al. Nitrogen availability increases in a tundra ecosystem during five years of experimental permafrost thaw. Glob Chang Biol. 2016;22(5):1927-41.
4. Terrer C, Jackson RB, Prentice IC, Keenan TF, Kaiser C, Vicca S, et al. Nitrogen and phosphorus constrain the CO2 fertilization of global plant biomass. Nature Climate Change. 2019;9(9):684-9.
5. Landeweert R, Hoffland E, Finlay RD, Kuyper TW, Breemen Nv. Linking plants to rocks: ectomycorrhizal fungi mobilize nutrients from minerals. TRENDS in Ecology & Evolution. 2001;16(5):248-54.
6. Chapin III FS, Barsdate RJ, Barel D. Phosphorus Cycling in Alaskan Coastal Tundra: A Hypothesis for the Regulation of Nutrient Cycling. Oikos. 1978;31(2):189-99.
7. Zhu Q, Riley WJ, Tang J, Koven CD. Multiple soil nutrient competition between plants, microbes, and mineral surfaces: model development, parameterization, and example applications in several tropical forests. Biogeosciences. 2016;13(1):341-63.
8. Du E, Terrer, C., Pellegrini, A. F., Ahlström, A., van Lissa, C. J., Zhao, X., Xia, N., Wu, X. & Jackson, R. B. Global patterns of terrestrial nitrogen and phosphorus limitation. Nature Geoscience. 2020:1-6.
9. Giesler R, Esberg C, Lagerström A, Graae BJ. Phosphorus availability and microbial respiration across different tundra vegetation types. Biogeochemistry. 2011;108(1-3):429-45.
10. Shaver GR, Johnson LC, Cades DH, Murray G, Laundre JA, Rastetter EB, et al. Biomass and CO2 flux in wet sedge tundras: responses to nutrients, temperature, and light. Ecological Monographs. 1998;68(1):75-97.
11. Street LE, Mielke N, Woodin SJ. Phosphorus Availability Determines the Response of Tundra Ecosystem Carbon Stocks to Nitrogen Enrichment. Ecosystems. 2017;21(6):1155-67.
12. Slavik K, Peterson BJ, Deegan LA, Bowden WB, Hershey AE, Hobbie JE. Long-term responses of the Kuparuk River ecosystem to phosphorus fertilization. Ecology. 2004;85(4):939-54.
13. Peterson BJ, Hobbie, J.E., Hershey, A.E., Lock, M.A., Ford, T.E., Vestal, J.R., McKinley, V.L., Hullar, M.A., Miller, M.C., Ventullo, R.M., Volk, G.S. Transformation of a tundra river from heterotrophy to autotrophy by addition of phosphorus. Science. 1985;229(4720):1383-6.
14. Harms TK, Ludwig SM. Retention and removal of nitrogen and phosphorus in saturated soils of arctic hillslopes. Biogeochemistry. 2016;127(2-3):291-304.
15. Bekryaev RV, Polyakov IV, Alexeev VA. Role of Polar Amplification in Long-Term Surface Air Temperature Variations and Modern Arctic Warming. Journal of Climate. 2010;23(14):3888-906.
16. Khare N, Martin JD, Hesterberg D. Phosphate bonding configuration on ferrihydrite based on molecular orbital calculations and XANES fingerprinting. Geochimica et Cosmochimica Acta. 2007;71:4405–15.
17. Wang X, Liu F, Tan W, Li W, Feng X, Sparks DL. Characteristics of Phosphate Adsorption-Desorption Onto Ferrihydrite. Soil Science. 2013;178(1):1-11.

18. Walker TW, Syers JK. The fate of phosphorus during pedogenesis. Geoderma. 1976;15:1-19.
19. Vitousek PM, Porder S, Houlton BZ, Chadwick OA. Terrestrial phosphorus limitation: mechanisms, implications, and nitrogen–phosphorus interactions. Ecological Applications. 2010;20(1):5-15.
20. Lipson DA, Jha M, Raab TK, Oechel WC. Reduction of iron (III) and humic substances plays a major role in anaerobic respiration in an Arctic peat soil. Journal of Geophysical Research. 2010;115.
21. Lipson DA, Zona D, Raab TK, Bozzolo F, Mauritz M, Oechel WC. Water-table height and microtopography control biogeochemical cycling in an Arctic coastal tundra ecosystem. Biogeosciences. 2012;9(1):577-91.
22. Emerson D, Scott JJ, Benes J, Bowden WB. Microbial iron oxidation in the Arctic tundra and its implications for biogeochemical cycling. Appl Environ Microbiol. 2015;81(23):8066-75.
23. Lipson DA, Raab TK, Goria D, Zlamal J. The contribution of Fe(III) and humic acid reduction to ecosystem respiration in drained thaw lake basins of the Arctic Coastal Plain. Global Biogeochemical Cycles. 2013;27(2):399-409.
24. Roy Chowdhury T, Herndon EM, Phelps TJ, Elias DA, Gu B, Liang L, et al. Stoichiometry and temperature sensitivity of methanogenesis and CO2 production from saturated polygonal tundra in Barrow, Alaska. Glob Chang Biol. 2015;21(2):722-37.
25. Herndon EM, Mann BF, Roy Chowdhury T, Yang Z, Wullschleger SD, Graham D, et al. Pathways of anaerobic organic matter decomposition in tundra soils from Barrow, Alaska. Journal of Geophysical Research: Biogeosciences. 2015;120(11):2345-59.
26. Miller K, Lai C-T, Dahlgren R, Lipson D. Anaerobic Methane Oxidation in High-Arctic Alaskan Peatlands as a Significant Control on Net CH4 Fluxes. Soil Systems. 2019;3(1).
27. Herndon EM, Yang Z, Bargar J, Janot N, Regier TZ, Graham DE, et al. Geochemical drivers of organic matter decomposition in arctic tundra soils. Biogeochemistry. 2015;126(3):397-414.
28. Page SE, Kling GW, Sander M, Harrold KH, Logan JR, McNeill K, et al. Dark formation of hydroxyl radical in Arctic soil and surface waters. Environ Sci Technol. 2013;47(22):12860-7.
29. Trusiak A, Treibergs LA, Kling GW, Cory RM. The role of iron and reactive oxygen species in the production of CO2 in arctic soil waters. Geochimica et Cosmochimica Acta. 2018;224:80-95.
30. Herndon E, AlBashaireh A, Singer D, Roy Chowdhury T, Gu B, Graham D. Influence of iron redox cycling on organo-mineral associations in Arctic tundra soil. Geochimica et Cosmochimica Acta. 2017;207:210-31.
31. Mueller CW, Hoeschen C, Steffens M, Buddenbaum H, Hinkel K, Bockheim JG, et al. Microscale soil structures foster organic matter stabilization in permafrost soils. Geoderma. 2017;293:44-53.
32. Jensen HS, Kristensen P, Jeppesen E, Skytthe A. Iron:phosphorus ratio in surface sediment as an indicator of phosphate release from aerobic sediments in shallow lakes. Hydrobiologia. 1992;235/236:731-43.
33. Zak D, Gelbrecht J, Steinberg CEW. Phosphorus retention at the redox interface of peatlands adjacent to surface waters in northeast Germany. Biogeochemistry. 2004;7:357–68.
34. Kinsman-Costello LE, O'Brien J, Hamilton SK. Re-flooding a Historically Drained Wetland Leads to Rapid Sediment Phosphorus Release. Ecosystems. 2014;17(4):641-56.
35. Olander LP, Vitousek PM. Biological and Geochemical Sinks for Phosphorus in Soil from a Wet Tropical Forest. Ecosystems. 2004;7(4).
36. Lin Y, Bhattacharyya A, Campbell AN, Nico PS, Pett-Ridge J, Silver WL. Phosphorus Fractionation Responds to Dynamic Redox Conditions in a Humid Tropical Forest Soil. Journal of Geophysical Research: Biogeosciences. 2018;123(9):3016-27.

37. Gross A, Lin Y, Weber PK, Pett-Ridge J, Silver WL. The role of soil redox conditions in microbial phosphorus cycling in humid tropical forests. Ecology. 2020;101(2):e02928.
38. Weintraub MN. Biological Phosphorus Cycling in Arctic and Alpine Soils. Phosphorus in Action. Soil Biology2011. p. 295-316.
39. Herndon EM, Kinsman-Costello L, Duroe KA, Mills J, Kane ES, Sebestyen SD, et al. Iron (Oxyhydr)Oxides Serve as Phosphate Traps in Tundra and Boreal Peat Soils. Journal of Geophysical Research: Biogeosciences. 2019;124(2):227-46.
40. Keuper F, Dorrepaal E, van Bodegom PM, van Logtestijn R, Venhuizen G, van Hal J, et al. Experimentally increased nutrient availability at the permafrost thaw front selectively enhances biomass production of deep-rooting subarctic peatland species. Glob Chang Biol. 2017;23(10):4257-66.
41. Zhu Q, Iversen CM, Riley WJ, Slette IJ, Vander Stel HM. Root traits explain observed tundra vegetation nitrogen uptake patterns: Implications for trait-based land models. Journal of Geophysical Research: Biogeosciences. 2016;121(12):3101-12.
42. Hewitt RE, Taylor DL, Genet H, McGuire AD, Mack MC, Mariotte P. Below-ground plant traits influence tundra plant acquisition of newly thawed permafrost nitrogen. Journal of Ecology. 2019;107(2):950-62.
43. Salmon VG, Schädel C, Bracho R, Pegoraro E, Celis G, Mauritz M, et al. Adding Depth to Our Understanding of Nitrogen Dynamics in Permafrost Soils. Journal of Geophysical Research: Biogeosciences. 2018;123(8):2497-512.
44. Wullschleger SD, Hinzman LD, Wilson CJ. Planning the Next Generation of Arctic Ecosystem Experiments. Eos. 2011;90(17):145.
45. Western Regional Climate Center, Barrow Post Rogers AP, Alaska (500546) [Internet]. 2020 [cited March 15, 2020.].
46. Hinkel KM, Eisner WR, Bockheim JG, Nelson FE, Peterson KM, Dai X. Spatial Extent, Age, and Carbon Stocks in Drained Thaw Lake Basins on the Barrow Peninsula, Alaska. Arctic, Antarctic, and Alpine Research. 2003;35(3):291-300.
47. Hubbard SS, Gangodagamage C, Dafflon B, Wainwright H, Peterson J, Gusmeroli A, et al. Quantifying and relating land-surface and subsurface variability in permafrost environments using LiDAR and surface geophysical datasets. Hydrogeology Journal. 2013;21(1):149-69.
48. Zona D, Lipson DA, Zulueta RC, Oberbauer SF, Oechel WC. Microtopographic controls on ecosystem functioning in the Arctic Coastal Plain. Journal of Geophysical Research. 2011;116.
49. Newman BD, Throckmorton HM, Graham DE, Gu B, Hubbard SS, Liang L, et al. Microtopographic and depth controls on active layer chemistry in Arctic polygonal ground. Geophysical Research Letters. 2015;42(6):1808-17.
50. Norby RJ, Sloan VL, Iversen CM, Childs J. Controls on Fine-Scale Spatial and Temporal Variability of Plant-Available Inorganic Nitrogen in a Polygonal Tundra Landscape. Ecosystems. 2019;22(3):528-43.
51. Menacherry SPM, Kim K, Lee W, Choi CH, Choi W. Ligand-Specific Dissolution of Iron Oxides in Frozen Solutions. Environ Sci Technol. 2018;52(23):13766-73.
52. Herndon E, Kinsman-Costello L, Di-Domenico N, Duroe K, Barczok M, Wullschleger CS. Iron and Phosphorus Geochemistry in High-Centered and Low-Centered Polygon Soils from the Barrow Environmental Observatory, Utqiagvik, Alaska, 2015. Next Generation Ecosystem Experiments

Arctic Data Collection. Oak Ridge National Laboratory, U.S. Department of Energy, Oak Ridge, Tennessee, USA. 2020.
53. Rayment GE, Higginson FR. Australian laboratory handbook of soil and water chemical methods.: Inkata Press Pty Ltd.; 1992.
54. Gardner WH. Water content. Methods of Soil Analysis: Part 1 Physical and Mineralogical Methods. 51986. p. 493-544.
55. Bockheim JG, Hinkel KM, Nelson FE. Predicting Carbon Storage in Tundra Soils of Arctic Alaska. Soil Sci Soc Am J. 2003;67:948–50.
56. Siregar A, Kleber M, Mikutta R, Jahn R. Sodium hypochlorite oxidation reduces soil organic matter concentrations without affecting inorganic soil constituents. European Journal of Soil Science. 2005;56(4):481-90.
57. Amacher MC, Henderson RE, Breithaupt MD, Seale CL, LaBauve JM. Unbuffered and buffered salt methods for exchangeable cations and effective cation-exchange capacity. Soil Science Society of America Journal. 1990;54(4):1036-42.
58. Poulton SW, Canfield DE. Development of a sequential extraction procedure for iron: implications for iron partitioning in continentally derived particulates. Chemical Geology. 2005;214(3-4):209-21.
59. Paludan C, Jensen HS. Sequential extraction of phosphorus in freshwater wetland and lake sediment: significance of humic acids. Wetlands. 1995;15(4):365-73.
60. Prietzel J, Harrington G, Hausler W, Heister K, Werner F, Klysubun W. Reference spectra of important adsorbed organic and inorganic phosphate binding forms for soil P speciation using synchrotron-based K-edge XANES spectroscopy. J Synchrotron Radiat. 2016;23(2):532-44.
61. McKeague JA, Day JH. Dithionite and oxalate extractable Fe and Al as aids in differentiating various classes of soils. Canadian Journal of Soil Science. 1966;46:13-22.
62. Kostka JE, Luther III GW. Partitioning and speciation of solid phase iron in saltmarsh sediments. Geochimica et Cosmochimica Acta. 1994;58(7):1701-10.
63. Bache BW, Williams EG. A phosphate sorption index for soils. Journal of Soil Science. 1971;22(3):289-301.
64. Ravel B, Newville M. ATHENA, ARTEMIS, HEPHAESTUS: data analysis for X-ray absorption spectroscopy using IFEFFIT. J Synchrotron Radiat. 2005;12(Pt 4):537-41.
65. Liljedahl AK, Hinzman LD, Schulla J, editors. Ice wedge polygon type controls low-gradient watershed-scale hydrology. Proceedings of the Tenth International Conference on Permafrost; 2012; Salekhard, Russia: The Northern Publisher.
66. Lara MJ, McGuire AD, Euskirchen ES, Tweedie CE, Hinkel KM, Skurikhin AN, et al. Polygonal tundra geomorphological change in response to warming alters future CO2 and CH4 flux on the Barrow Peninsula. Glob Chang Biol. 2015;21(4):1634-51.
67. Bethke CM, Sanford RA, Kirk MF, Jin Q, Flynn TM. The thermodynamic ladder in geomicrobiology. American Journal of Science. 2011;311(3):183-210.
68. Karlsson T, Persson P, Skyllberg U, Morth C-M, Giesler R. Characterization of Iron(III) in Organic Soils Using Extended X-ray Absorption Fine Structure Spectroscopy. Environmental Science and Technology. 2008;42:5449–54.
69. Karlsson T, Persson P. Coordination chemistry and hydrolysis of Fe(III) in a peat humic acid studied by X-ray absorption spectroscopy. Geochimica et Cosmochimica Acta. 2010;74(1):30-40.
70. Sundman A, Karlsson T, Laudon H, Persson P. XAS study of iron speciation in soils and waters from a boreal catchment. Chemical Geology. 2014;364:93-102.

71. O'Day PA, Rivera N, Root R, Carroll SA. X-ray absorption spectroscopic study of Fe reference compounds for the analysis of natural sediments. American Mineralogist. 2004;89(4):572-85.
72. Giblin AE, Nadelhoffer KJ, Shaver GR, Laundre JA, McKerrow AJ. Biogeochemical diversity along a riverside toposequence in arctic Alaska. Ecological Monographs. 1991;61(4):415-35.
73. Henderson R, Kabengi N, Mantripragada N, Cabrera M, Hassan S, Thompson A. Anoxia-induced release of colloid- and nanoparticle-bound phosphorus in grassland soils. Environ Sci Technol. 2012;46(21):11727-34.
74. Bhattacharyya A, Campbell AN, Tfaily MM, Lin Y, Kukkadapu RK, Silver WL, et al. Redox Fluctuations Control the Coupled Cycling of Iron and Carbon in Tropical Forest Soils. Environ Sci Technol. 2018;52(24):14129-39.
75. Smits MM, Bonneville S, Benning LG, Banwart SA, Leake JR. Plant-driven weathering of apatite--the role of an ectomycorrhizal fungus. Geobiology. 2012;10(5):445-56.
76. Jobbágy EJ, Jackson RB. The distribution of soil nutrients with depth: Global patterns and the imprint of plants. Biogeochemistry. 2001;53:51-77.
77. Fiedler S, Wagner D, Kutzbach L, Pfeiffer E-M. Element Redistribution along Hydraulic and Redox Gradients of Low-Centered Polygons, Lena Delta, Northern Siberia. Soil Sci Soc Am J. 2005;68:1002-11.
78. Adhikari D, Zhao Q, Das K, Mejia J, Huang R, Wang X, et al. Dynamics of ferrihydrite-bound organic carbon during microbial Fe reduction. Geochimica et Cosmochimica Acta. 2016;212:221-33.
79. Shimizu M, Zhou J, Schroder C, Obst M, Kappler A, Borch T. Dissimilatory reduction and transformation of ferrihydrite-humic acid coprecipitates. Environ Sci Technol. 2013;47(23):13375-84.
80. Jones DL. Organic acids in the rhizosphere – a critical review. Plant and Soil. 1998;205:25-44.
81. Hicks Pries CE, Schuur EA, Crummer KG. Thawing permafrost increases old soil and autotrophic respiration in tundra: partitioning ecosystem respiration using delta(13) C and (14) C. Glob Chang Biol. 2013;19(2):649-61.
82. Colmer TD. Long-distance transport of gases in plants: a perspective on internal aeration and radial oxygen loss from roots. Plant, Cell and Environment 2003;26:17-36.
83. Visser EJW, Colmer TD, Blom CWPM, Voesenek LACJ. Changes in growth, porosity, and radial oxygen loss from adventitious roots of selected mono- and dicotyledonous wetland species with contrasting types of aerenchyma. Plant, Cell and Environment. 2000;23:1237–45.
84. Iversen CM, Sloan VL, Sullivan PF, Euskirchen ES, McGuire AD, Norby RJ, et al. The unseen iceberg: plant roots in arctic tundra. New Phytol. 2015;205(1):34-58.
85. Brantley SL, Lebedeva M. Learning to Read the Chemistry of Regolith to Understand the Critical Zone. Annual Review of Earth and Planetary Sciences. 2011;39(1):387-416

Table 1. Chemical and physical properties of the bulk soil horizons (mean ± standard error of the mean; n = 3)

Polygon	Feature	Horizon	Depth (cm)	Soil pH	N (wt%)	C (wt%)	VWC[a] (cm^3 cm^{-3})	LOI (%)
High-centered	Center	Organic	0 (± 0) – 11 (± 1)	3.93 ± 0.06	1.61 ± 0.25	39.5 ± 3.6	0.12 ± 0.02	75.5 ± 6.5
		Mineral	11 (± 1) – 28 (± 1)	4.20 ± 0.06	0.65 ± 0.16	12.6 ± 3.4	0.32 ± 0.05	21.6 ± 6.5
High-centered	Trough	Organic	0 (± 0) – 11 (± 2)	4.98 ± 0.08	1.43 ± 0.05	32.7 ± 2.7	0.42 ± 0.02	64.9 ± 6.5
		Mineral	11 (± 2) – 26 (± 2)	5.09 ± 0.15	0.76 ± 0.08	23.3 ± 10.8	0.44 ± 0.19	38.3 ± 12.7
Low-centered	Center	Organic	0 (± 0) – 14 (± 2)	4.36 ± 0.12	1.41 ± 0.47	26.0 ± 9.4	0.36 ± 0.12	48.3 ± 19.3
Low-centered	Ridge	Organic	0 (± 0) – 8 (± 0.3)	4.06 ± 0.01	1.80 ± 0.12	42.5 ± 0.5	0.12 ± 0.02	89.6 ± 2.3
		Mineral	8 (± 0.3) – 20 (± 1)	4.12 ± 0.01	0.86 ± 0.07	16.4 ± 1.0	0.40 ± 0.02	32.7 ± 1.9
Low-centered	Trough	Organic	0 (± 0) – 12 (± 0)	4.90 ± 0.10	1.47 ± 0.34	29.7 ± 7.7	0.57 ± 0.17	56.7 ± 17.2
		Mineral	12 (± 0) – 20 (± 0.3)	4.85 ± 0.05	0.73 ± 0.13	13.8 ± 3.3	0.59 ± 0.04	27.3 ± 6.7

[a] Volumetric water content was calculated from gravimetric water content and bulk density

Table 2. Soil Fe for each polygon feature and horizon (mean ± std. err.) extracted as exchangeable, organic-bound, short-range ordered oxyhydroxides, or crystalline oxides

Polygon/Feature	**Horizon**	**Exchangeable** mmol kg^{-1}	**Organic-bound** mmol kg^{-1}	**SRO oxide** mmol kg^{-1}	**Crystalline** mmol kg^{-1}	**Total Extracted Fe** mmol kg^{-1}
HC-Center	Organic	5.81 ± 5.42	108.7 ± 47.3	73.1 ± 29.6	14.6 ± 5.0	202 ± 55
	Mineral	7.69 ± 5.83	33.8 ± 11.3	61.4 ± 8.7	23.5 ± 6.1	126 ± 11
HC-Trough	Organic	95.0 ± 70.3	131 ± 26	264 ± 191	27.4 ± 18.1	517 ± 289
	Mineral	54.5 ± 2.8	48.8 ± 5.2	83.1 ± 31.7	33.0 ± 16.2	192 ± 64
LC-Center	Organic	33.2 ± 14.8	66.8 ± 20.3	78.7 ± 36.6	15.5 ± 6.2	194 ± 36
LC-Ridge	Organic	10.0 ± 2.24	281 ± 19	259 ± 112	12.9 ± 2.8	563 ± 111
	Mineral	1.70 ± 1.23	69.2 ± 8.3	62.8 ± 11.4	20.7 ± 8.1	154 ± 13
LC-Trough	Organic	137 ± 38	113 ± 34	65.7 ± 20.6	20.1 ± 5.1	336 ± 82
	Mineral	69.6 ± 12.8	22.0 ± 3.2	35.1 ± 7.5	20.4 ± 6.6	147 ± 6
Low features	Organic	88.3 ± 27.9	104 ± 17	136 ± 65	21.0 ± 6.0	349 ± 99
	Mineral	63.6 ± 8.0	35.4 ± 6.6	59.1 ± 18.1	26.7 ± 8.3	165 ± 23
High features	Organic	7.91 ± 2.79	195 ± 45	166 ± 66	13.7 ± 2.6	383 ± 98
	Mineral	4.69 ± 2.98	51.5 ± 10.1	62.1 ± 6.4	22.1 ± 4.6	140 ± 10

Table 3. Iron oxidation state and proportions of major Fe-bearing components in a bulk soil horizon from each feature

Site	Horizon	E^0 eV (±0.5)	Ave. Fe Valence	XANES Red. χ^2	Fe^{II}-oxalate %	Fe^{III}-oxalate %	Fe^{III}-citrate %	Ferrihydrite %	Chlorite %	k^2 Red. χ^2
HC-Center	Organic	7125.4	2.89	0.087	11	2	40	34	13	0.009
	Mineral	7124.0	2.82	0.026	0	16	15	38	31	0.004
HC-Trough	Organic	7123.6	2.79	0.187	3	13	2	59	23	0.013
	Mineral	7123.1	2.77	0.084	0	0	16	58	26	0.018
LC-Center	Organic	7123.4	2.72	0.029	0	12	29	41	18	0.007
LC-Ridge	Organic	7124.1	2.87	0.099	0	0	26	63	11	0.023
	Mineral	7123.5	2.78	0.059	0	0	33	43	24	0.010
LC-Trough	Organic	7124.0	2.85	0.027	0	2	45	39	14	0.010
	Mineral	7123.0	2.68	0.032	0	2	28	34	35	0.005

Table 4. Soil phosphate sorption indices (PSI) and P concentrations (mean ± std. err. mean) extracted as water-soluble P_i, dithionite-soluble P_i, base-soluble P_i, acid-soluble P, or organic P for each landscape feature and horizon

Site	Horizon	PSI	Water-P_i	Dithionite-P_i	Base-P_i	Acid-P	Organic-P	Total Extracted P
			mmol kg^{-1}	mmol kg^{-1}	mmol kg^{-1}	mmol kg^{-1}	mmol kg^{-1}	mmol kg^{-1}
HC-Center	Organic	34.4 ± 6.03	0.17 ± 0.08	1.37 ± 1.20	1.82 ± 1.16	3.59 ± 2.40	5.14 ± 4.12	12.1 ± 4.01
	Mineral	32.0 ± 3.39	0.02 ± n.a.	0.06 ± n.a.	0.57 ± n.a.	5.17 ± n.a.	0.85 ± n.a.	6.68 ± n.a.
HC-Trough	Organic	63.3 ± 9.19	0.22 ± 0.14	3.23 ± 0.22	4.08 ± 1.27	1.22 ± 1.06	5.56 ± 2.04	14.3 ± 1.91
	Mineral	48.5 ± 8.21	1.18 ± n.a.	0.71 ± n.a.	1.89 ± n.a.	0.24 ± n.a.	4.18 ± n.a.	9.75 ± 4.57
LC-Center	Organic	50.9 ± 6.17	0.34 ± 0.29	1.98 ± 1.79	4.19 ± 2.65	0.95 ± 0.78	2.27 ± 0.62	15.3 ± 1.93
LC-Ridge	Organic	80.0 ± 11.3	1.22 ± 0.84	4.41 ± 0.08	7.97 ± 1.21	0.10 ± 0.09	1.36 ± 0.07	8.76 ± 0.30
	Mineral	37.9 ± 2.44	0.02 ± 0.00	0.57 ± 0.23	1.25 ± 0.13	5.01 ± 0.11	1.89 ± 0.18	14.7 ± 6.78
LC-Trough	Organic	86.1 ± 28.5	0.39 ± 0.25	3.77 ± 2.90	5.72 ± 3.03	1.56 ± 0.25	3.29 ± 0.85	8.18 ± 0.24
	Mineral	41.9 ± 9.07	0.03 ± 0.00	0.41 ± 0.11	1.02 ± 0.00	3.44 ± 0.75	3.27 ± 0.37	12.1 ± 4.01
Low features	Organic	66.8 ± 10.2	0.32 ± 0.11	2.99 ± 0.94	4.66 ± 1.14	1.24 ± 0.36	3.71 ± 0.85	12.9 ± 2.39
	Mineral	44.5 ± 5.83	0.41 ± 0.38	0.51 ± 0.12	1.31 ± 0.29	2.37 ± 1.15	3.58 ± 0.37	8.19 ± 0.14
High features	Organic	57.2 ± 11.7	0.69 ± 0.46	2.89 ± 1.00	4.89 ± 1.90	1.84 ± 1.40	3.25 ± 2.00	13.7 ± 2.03
	Mineral	35.0 ± 2.29	0.02 ± 0.00	0.40 ± 0.21	1.02 ± 0.24	5.06 ± 0.08	1.54 ± 0.36	8.07 ± 0.71

Figure 1. (a) The study area, indicated by the red square that corresponds to the area shown in panel (b), was located in the Barrow Environmental Observatory (BEO) outside of Utqiagvik, AK on the North Slope near the Arctic Ocean. (b) Tundra in the BEO contains areas of high-centered and low-centered ice-wedge polygons. Soil cores were collected in triplicate from (c) the center and trough positions of a high-centered polygon, and from (d) the center, ridge, and trough positions of a low-centered polygon. Schematics of the high-centered and low-centered polygon shown here were adapted from representative polygons described by Hubbard et al. (2013)[47] and do not show the specific polygons from which these cores were obtained. Elevation change and soil core length within the polygons are to scale with 10× vertical exaggeration relative to horizontal distance, as shown by the scale in panel (d). Core length equals thaw depth at time of collection. Aerial images from Google Earth.

Figure 2. Box-and-whisker plots of volumetric water content (cm^3 H_2O cm^{-3}) and soil pH for organic (light) and mineral (dark) horizons within each landscape feature. Boxes represent one standard error around the mean, shown as a white square, and whiskers span the entire data range. The median for each sample set is shown by a horizontal line within each box. All data points are shown as grey diamonds overlaying each box-and-whisker plot.

Figure 3. Box-and-whisker plots of the concentrations (mmol kg^{-1}) and proportions (%) of (1) extracted Fe in exchangeable, organic-bound, short-range ordered oxyhydroxide, and crystalline oxide phases; and (2) extracted P in water-soluble inorganic P (water-P_i), reducible iron-bound inorganic P (dithionite-P_i), non-reducible oxide-bound inorganic P (base-P_i), carbonate-associated inorganic P (acid-P), and organic P. Each box-and-whisker plot represents a topographic position (high or low) and a horizon (organic 'O' or mineral 'M'). Boxes represent one standard error around the mean, shown as a white square, and whiskers span the entire data range. Colors emphasize boxes associated with high (orange) or low (blue) features and organic (light) or mineral (dark) horizons. The median for each sample set is shown by a horizontal line. All data points are shown as jiggered grey diamonds overlaying each box-and-whisker plot. Asterisks below each fraction indicate p-values (* < 0.05; ** < 0.01; *** < 0.001) derived from two-way ANOVA for topography (*T*) and horizon (*H*). Letters indicate significant mean differences between sample sets within each fraction (Tukey's post-hoc test).

Figure 4. Iron K-edge x-ray absorption near edge structure (XANES) spectra (*left panels*) and major components reported from linear combination fits (*middle panels*) to the extended x-ray absorption fine structure (EXAFS) spectra of depth increments from complete soil cores (*right panels*). In the XANES plots, spectra from organic horizon soils are plotted in black and from mineral horizon soils are plotted in grey. Energy positions of white lines associated with Fe(II) (*blue*) and Fe(III) (*orange*) species are shown as vertical bars. For the EXAFS spectra, experimental data are shown in grey and best fit lines are shown in black. Lighter component bars indicate spectra for which fits were poor (red. $\chi^2 > 0.03$) (Table S5). Spectra and components for each core are arranged from the shallowest soil at the top to the deepest soil at the bottom, as indicated by the mid-point depths shown on the y-axis in the middle panels.

Figure 5. Concentrations (mmol kg^{-1}) of water-soluble and dithionite-soluble inorganic P (P_i), Fe, and Al versus soil depth in soils collected from across microtopographic features of high-centered and low-centered polygons. The approximate boundary between organic and mineral horizons (8 to 12 cm depth) is shown by the stippled grey bar. Open symbols in each panel indicate two soil intervals from the high-

centered polygon trough (HCT) with unique enrichment of metals at depth. Data from all soils are plotted together and include five complete cores (one per topographic feature) and select depth intervals from additional replicate cores.

Figure 6. (*left panel*) Representative depth profiles for water-soluble inorganic P, dithionite-soluble inorganic P, and dithionite-soluble Fe based on trends shown in Figure 5. (*right panel*) Conceptual diagram showing major biogeochemical pathways for Fe and P in organic and mineral horizons. Major P pathways include dissolution from primary minerals (e.g. apatite), phosphate uptake by plants, plant death and organic P formation, enzymatic release of phosphate from soil organic matter (SOM), microbial assimilation and release, and adsorption to Fe oxides. Major Fe pathways include dissolution from primary minerals (e.g., chlorite or other silicates), upward translocation to surface soils, oxidation, complexation with soil organic matter, and precipitation as Fe oxides.

Table of Contents

Iron accumulation in shallow tundra soils promotes adsorption of phosphate from soil solution, sequestering high concentrations of potentially bioavailable phosphorus.

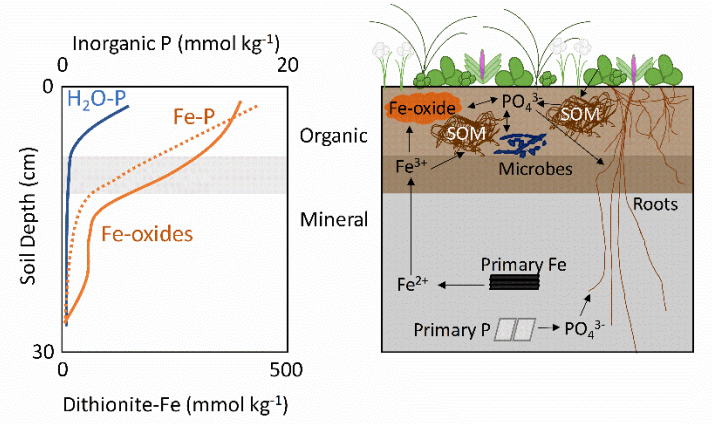

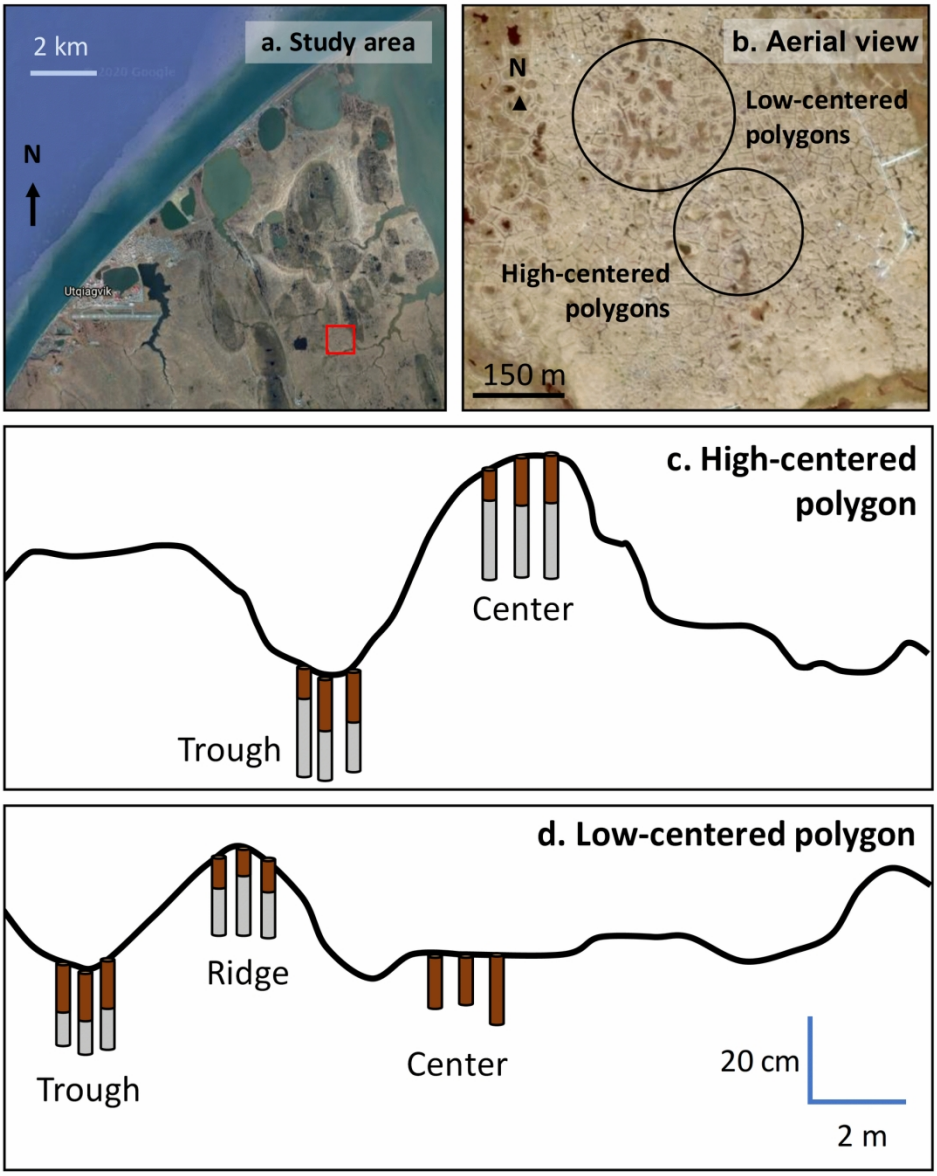

Figure 1. (a) The study area, indicated by the red square that corresponds to the area shown in panel (b), was located in the Barrow Environmental Observatory (BEO) outside of Utqiaġvik, AK on the North Slope near the Arctic Ocean. (b) Tundra in the BEO contains areas of high-centered and low-centered ice-wedge polygons. Soil cores were collected in triplicate from (c) the center and trough positions of a high-centered polygon, and from (d) the center, ridge, and trough positions of a low-centered polygon. Schematics of the high-centered and low-centered polygon shown here were adapted from representative polygons described by Hubbard et al. (2013)47 and do not show the specific polygons from which these cores were obtained. Elevation change and soil core length within the polygons are to scale with 10× vertical exaggeration relative to horizontal distance, as shown by the scale in panel (d). Core length equals thaw depth at time of collection. Aerial images from Google Earth.

165x203mm (300 x 300 DPI)

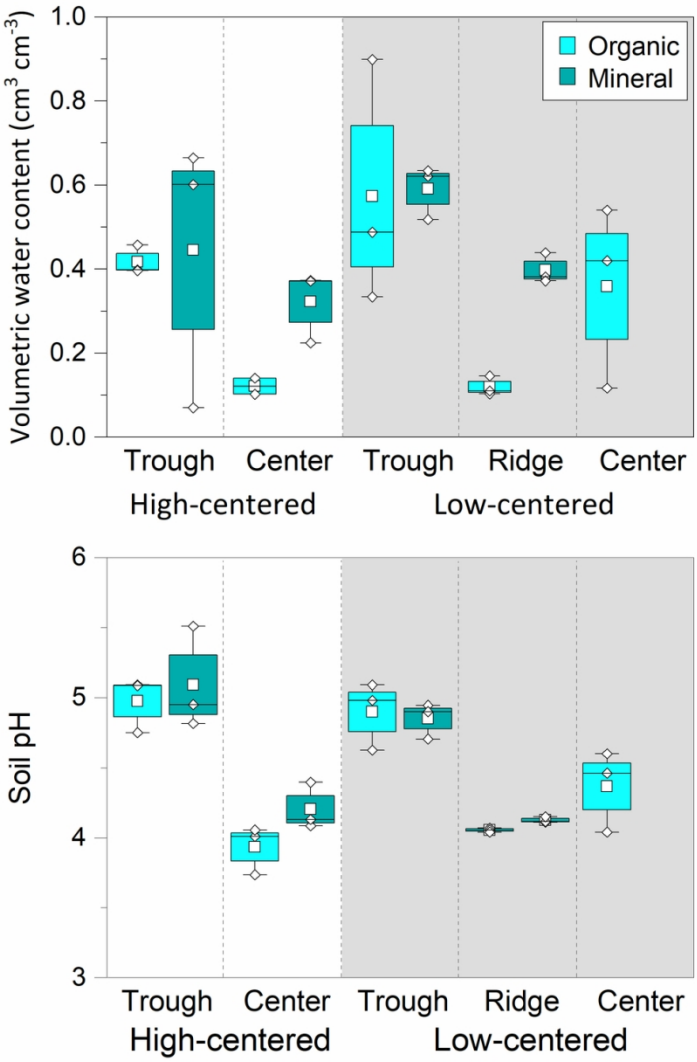

Figure 2. Box-and-whisker plots of volumetric water content (cm3 H2O cm-3) and soil pH for organic (light) and mineral (dark) horizons within each landscape feature. Boxes represent one standard error around the mean, shown as a white square, and whiskers span the entire data range. The median for each sample set is shown by a horizontal line within each box. All data points are shown as grey diamonds overlaying each box-and-whisker plot.

99x143mm (300 x 300 DPI)

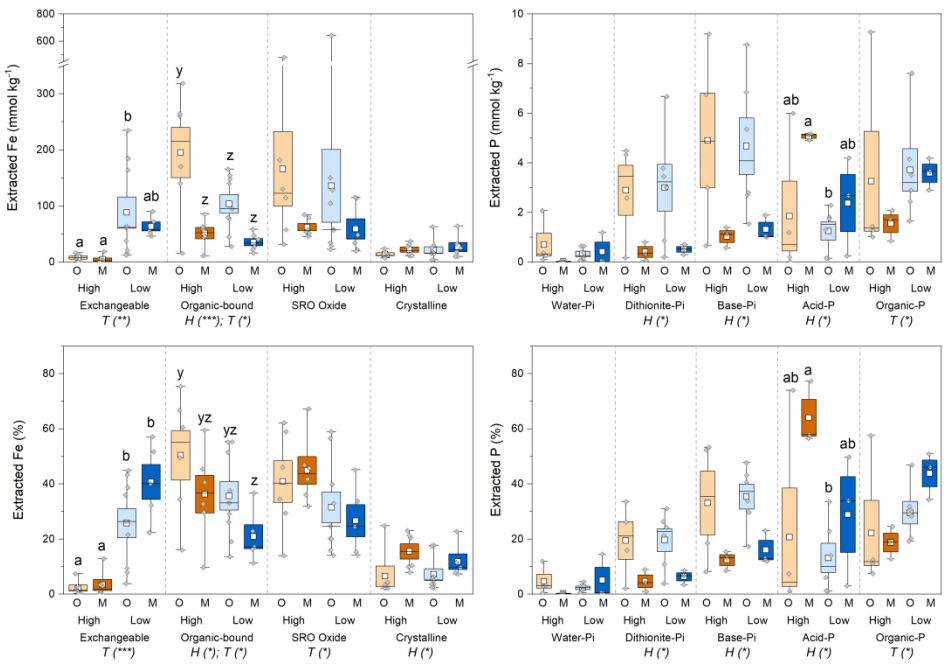

Figure 3. Box-and-whisker plots of the concentrations (mmol kg-1) and proportions (%) of (1) extracted Fe in exchangeable, organic-bound, short-range ordered oxyhydroxide, and crystalline oxide phases; and (2) extracted P in water-soluble inorganic P (water-Pi), reducible iron-bound inorganic P (dithionite-Pi), non-reducible oxide-bound inorganic P (base-Pi), carbonate-associated inorganic P (acid-P), and organic P. Each box-and-whisker plot represents a topographic position (high or low) and a horizon (organic 'O' or mineral 'M'). Boxes represent one standard error around the mean, shown as a white square, and whiskers span the entire data range. Colors emphasize boxes associated with high (orange) or low (blue) features and organic (light) or mineral (dark) horizons. The median for each sample set is shown by a horizontal line. All data points are shown as jiggered grey diamonds overlaying each box-and-whisker plot. Asterisks below each fraction indicate p-values (* < 0.05; ** < 0.01; *** < 0.001) derived from two-way ANOVA for topography (T) and horizon (H). Letters indicate significant mean differences between sample sets within each fraction (Tukey's post-hoc test).

170x119mm (600 x 600 DPI)

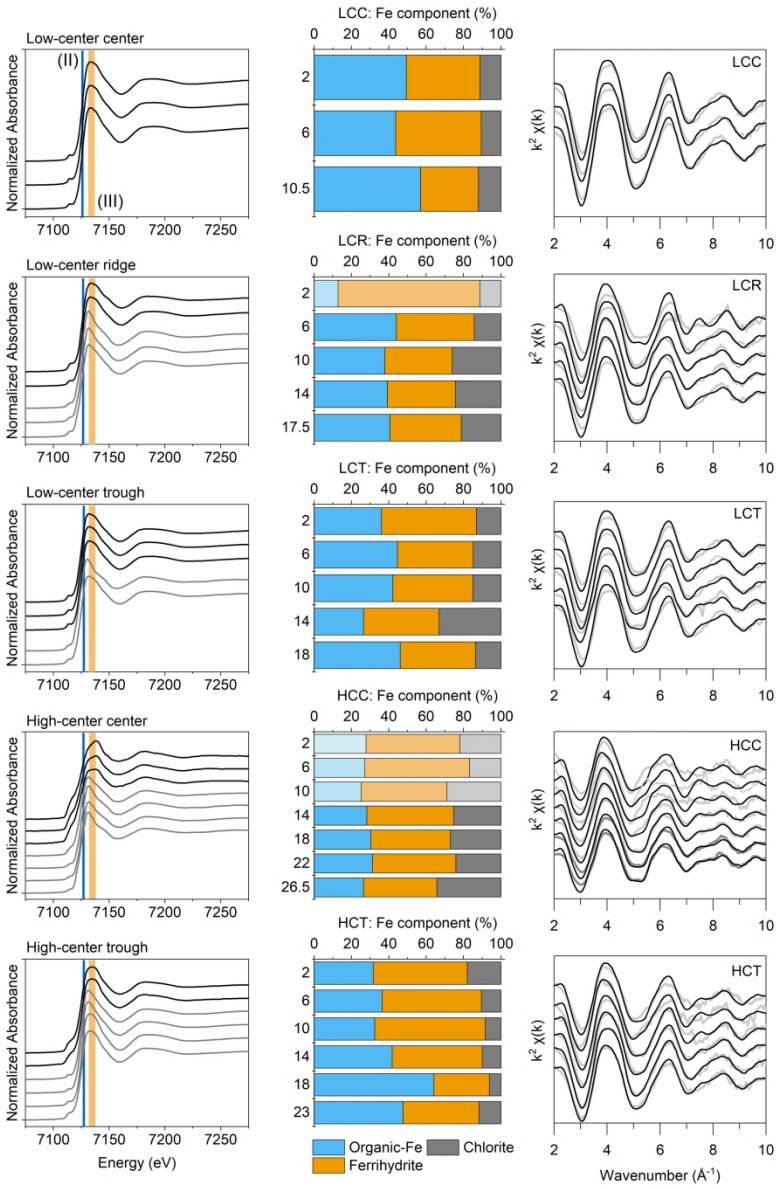

Figure 4. Iron K-edge x-ray absorption near edge structure (XANES) spectra (left panels) and major components reported from linear combination fits (middle panels) to the extended x-ray absorption fine structure (EXAFS) spectra of depth increments from complete soil cores (right panels). In the XANES plots, spectra from organic horizon soils are plotted in black and from mineral horizon soils are plotted in grey. Energy positions of white lines associated with Fe(II) (blue) and Fe(III) (orange) species are shown as vertical bars. For the EXAFS spectra, experimental data are shown in grey and best fit lines are shown in black. Lighter component bars indicate spectra for which fits were poor (red. $\chi 2 > 0.03$) (Table S5). Spectra and components for each core are arranged from the shallowest soil at the top to the deepest soil at the bottom, as indicated by the mid-point depths shown on the y-axis in the middle panels.

198x289mm (300 x 300 DPI)

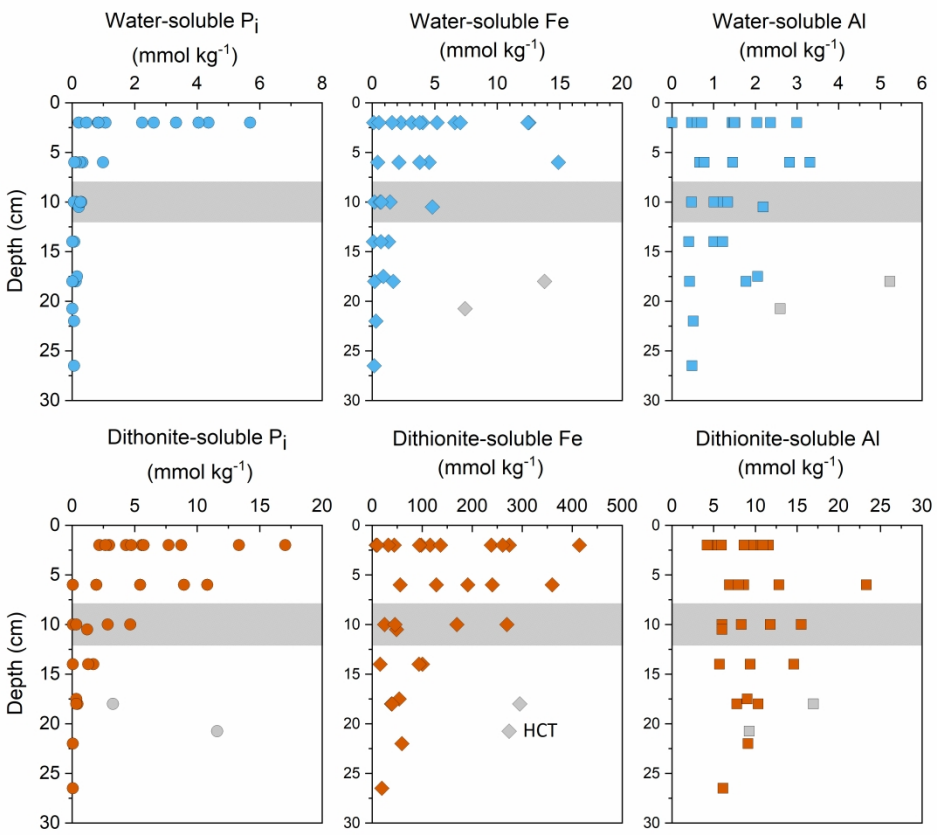

Figure 5. Concentrations (mmol kg-1) of water-soluble and dithionite-soluble inorganic P (Pi), Fe, and Al versus soil depth in soils collected from across microtopographic features of high-centered and low-centered polygons. The approximate boundary between organic and mineral horizons (8 to 12 cm depth) is shown by the stippled grey bar. Open symbols in each panel indicate two soil intervals from the high-centered polygon trough (HCT) with unique enrichment of metals at depth. Data from all soils are plotted together and include five complete cores (one per topographic feature) and select depth intervals from additional replicate cores.

170x149mm (600 x 600 DPI)

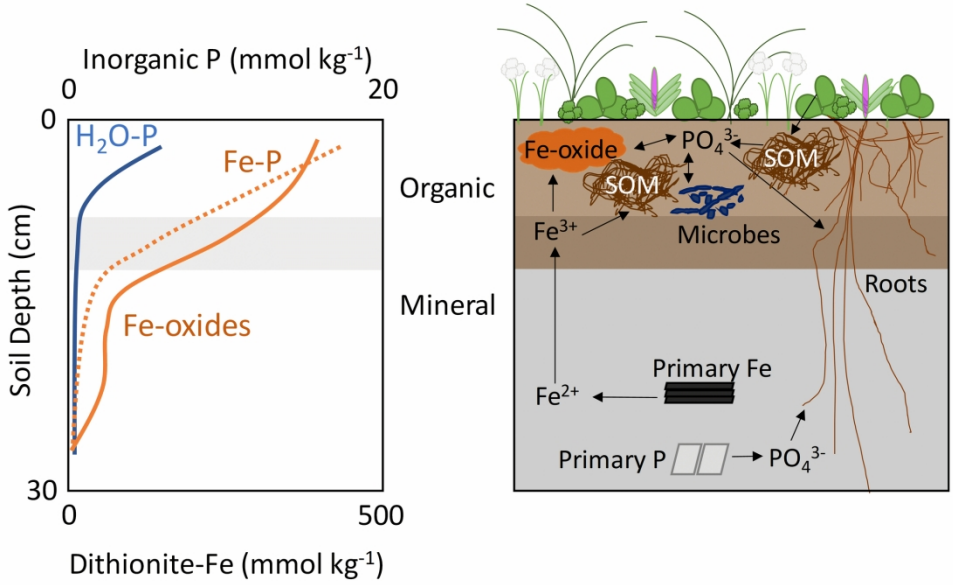

Figure 6. (left panel) Representative depth profiles for water-soluble inorganic P, dithionite-soluble inorganic P, and dithionite-soluble Fe based on trends shown in Figure 5. (right panel) Conceptual diagram showing major biogeochemical pathways for Fe and P in organic and mineral horizons. Major P pathways include dissolution from primary minerals (e.g. apatite), phosphate uptake by plants, plant death and organic P formation, enzymatic release of phosphate from soil organic matter (SOM), microbial assimilation and release, and adsorption to Fe oxides. Major Fe pathways include dissolution from primary minerals (e.g., chlorite or other silicates), upward translocation to surface soils, oxidation, complexation with soil organic matter, and precipitation as Fe oxides.

199x119mm (300 x 300 DPI)